

# We are IntechOpen, the world's leading publisher of Open Access books Built by scientists, for scientists

6,900

Open access books available

186,000

International authors and editors

200M

Downloads

Our authors are among the

154

Countries delivered to

TOP 1%

most cited scientists

12.2%

Contributors from top 500 universities



WEB OF SCIENCE™

Selection of our books indexed in the Book Citation Index  
in Web of Science™ Core Collection (BKCI)

Interested in publishing with us?  
Contact [book.department@intechopen.com](mailto:book.department@intechopen.com)

Numbers displayed above are based on latest data collected.  
For more information visit [www.intechopen.com](http://www.intechopen.com)



# On the Reliability of Diffusion Neuroimaging

Jan Klein, Sebastiano Barbieri, Hannes Stuke, Horst K. Hahn  
*Fraunhofer MEVIS  
Germany*

Miriam H. A. Bauer, Jan Egger, Christopher Nimsky  
*Dept. of Neurosurgery, University of Marburg  
Germany*

## 1. Introduction

Over the last years, diffusion imaging techniques like DTI, DSI or Q-Ball received increasing attention, especially in the neuroimaging, neurological, and neurosurgical community. An explicit geometrical reconstruction of major white matter tracts has become available by fiber tracking based on diffusion-weighted images. The goal of virtually all fiber tracking algorithms is to compute results which are analogous to what the physicians or radiologists are expecting and an extensive amount of research has therefore been focussed on this reconstruction. However, the results of fiber tracking and quantification algorithms are approximations of the reality due to limited spatial resolution (typically a few millimeters), model assumptions (e.g., diffusion assumed to be Gaussian distributed), user-defined parameter settings, and physical imaging artifacts resulting from diffusion sequences. In this book chapter, we will address the problem of uncertainty in diffusion imaging and we will show possible solutions for minimizing, measuring and visualizing the uncertainty.

The possibility of fiber tracking (FT) and the quantification of diffusion parameters has established an abundance of new clinically useful applications and research studies that focus on neurosurgical planning (Nimsky et al., 2005), monitoring the progression of diseases such as amyotrophic lateral sclerosis (ALS) or multiple sclerosis (MS) (Griffin et al., 2001), establishing surrogate markers used in assessing the grade of brain tumors (Barboriak, 2003), or initiating therapies to ensure the best possible development of children (Pul et al., 2006). Several studies have shown that modified values of fractional anisotropy (FA), relative anisotropy, or diffusion strength (ADC) are indicators of diseases that affect white matter tissue. MS lesions have been investigated by ROI-based analysis and voxel-wise FA comparisons by which FA changes have been shown to occur in areas containing lesions and in areas of normal-appearing white matter. Moreover, methods for tract-based quantification have been developed for which parameters are computed depending on the local curvature or geodesic distance from a user-defined origin. These methods allow to automatically determine DTI-derived parameters along fiber bundles and have already been used to mirror disease progression and executive function in MS (Fink et al., 2009).

Probabilistic methods (Friman et al., 2006) allow for tracking in regions of low anisotropy and are also used to provide a quantitative measure of the probability of the existence of a connection between two regions. These approaches aim at visualizing the uncertainty present

in the data by incorporating models of the acquisition process and noise. The uncertainty is assessed by tracking many possible paths originating from a single seed point and by taking the tensor uncertainty into account. Session reproducibility and subject variability of FT algorithms have been examined in (Heiervang et al., 2006). A first comparison of deterministic and probabilistic approaches, both guided solely by the primary eigenvector, in combination with functional localization of brain tumor patients has been given in (Berman et al., 2004).

## 2. Minimizing, Measuring and Visualizing the Uncertainty in Diffusion Imaging

Correctness, plausibility, and reliability of fiber tracking and quantification techniques have mainly been verified using histologic knowledge (Inglis et al., 1999). In some few animal studies, manganese has already been used as tracer to directly examine the diffusion process (Lin et al., 2001). First quantitative results with respect to precision, uncertainty and reproducibility have also been published (Basser & Pajevic, 2003; Behrens et al., 2003; Jones, 2003). (Behrens et al., 2003) estimate the local probability density using a model describing the diffusion process. The model is used to determine the probability of a connection between two points and, therefore, is used as a quantitative measure for the correctness of the fiber tracking results. (Jones, 2003) makes use of the bootstrapping method in order to compute cones of uncertainties showing a 95% confidence angle. (Basser & Pajevic, 2003) propose a Gaussian distribution that describes the variability of the tensors in the ideal case where the image is only disturbed by radio frequency background noise. In combination with bootstrapping, where the real variability is measured, they are able to benchmark the quality of DTI data. Thereby, wavelet-based methods help them to reduce noise and to preserve borders between different tissue classes.

Phantoms, modeling physically plausible fiber bundles that conform (partially) with human anatomy are important in order to examine different quantification algorithms with respect to the points mentioned above. A phantom must allow to steer the respective DTI data generation under controlled conditions, either using a real MR scanner (*physical phantom*) or by the help of software in a simulation setup (*software phantom*).

Hardware phantoms to assess DTI can be created from physical materials such as silk threads or dialysis tubes (Fieremans, De Deene, Delputte, Ozdemir, Achten & Lemahieu, 2008) and placed in a water basin for acquiring the diffusion weighted images. Hardware phantom experiments for high angular resolution diffusion-weighted imaging (HARDI) data have been proposed recently (Tournier et al., 2008). In (Tournier et al., 2008) three different techniques are compared, namely constrained spherical deconvolution (CSD), super-resolved CSD and Q-ball imaging. It is shown that fiber tracking results, and as a consequence DTI quantification, depend on the employed algorithm's ability to resolve crossing fibers, and to provide accurate estimates of their orientations.

In contrast to hardware phantoms, software phantoms allow for an easy an exact geometrical description of arbitrarily shaped fibers and of an automatic computation of the corresponding diffusion weighted-images so that no MR scanner is needed. (Basser et al., 2002) describe fibers by simple 2D rings in tensor fields, whereas other authors (Gössl et al., 2002) define fibers by cylindrical tubes in 3D tensor fields. Thereby, tracts are defined by circular helices. A mathematical framework for simulating the partial volume between fiber and background tissue has been proposed in (Leemans et al., 2005). The authors obtain a model of a fiber bundle by parameterizing the various features which characterize the bundle. Their results show that a higher correspondence between experimental and synthetic DTI data exists when the modeling a nonconstant fiber density across bundles.

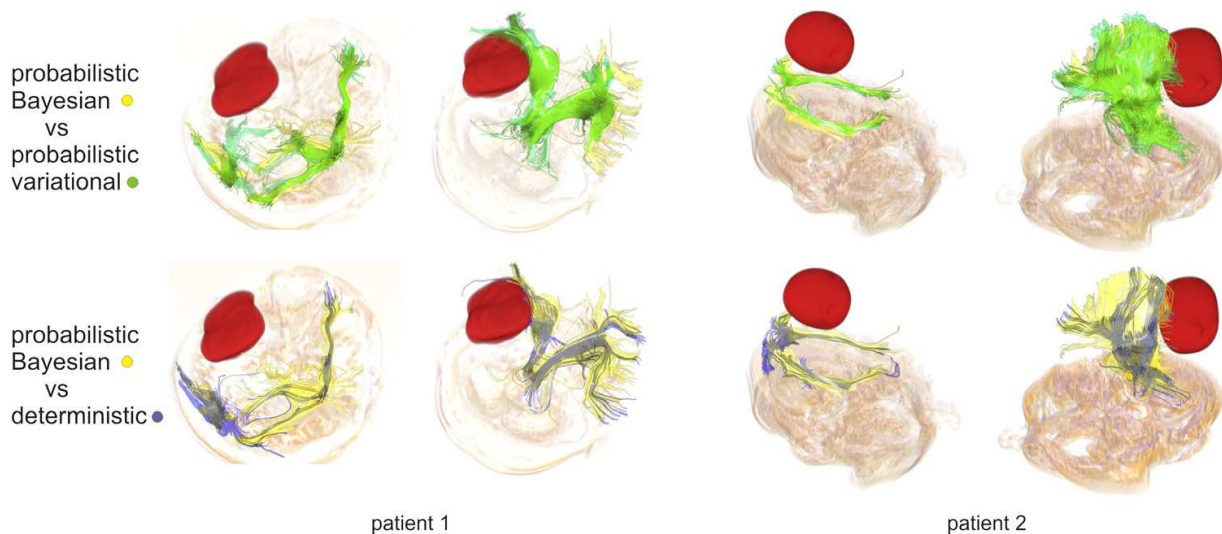


Fig. 1. Qualitative comparisons of fiber tracking for two glioma patients (Klein et al., 2010). We tracked two important structures, the pyramidal tract and the optical tract. Patient 1: frontotemporal glioma (grade 4), patient 2: progressive astrocytoma (grade 2).

In the following sections, we will go into more detail and will give several examples. Section 3 describes how uncertainty due to different tracking algorithms can be visualized and quantified. The next section will illustrate a software phantom for estimating the boundary of tracked fiber bundles. Section 5 summarizes an alternative algorithm for computing a safety hull around the fibers. Finally, we present a new algorithm for visualizing the uncertainty of the reconstruction by the fiber orientation distribution function (fODF), which is a probability distribution on a sphere.

### 3. Comparing Probabilistic and Deterministic Fiber Tracking

In the following, we will summarize our experiences with comparing probabilistic and deterministic fiber tracking (Klein et al., 2010) and will show which algorithm should be used under which circumstances. For that purpose, we focus on two patient groups: glioma patients and MS patients. Whereas tumors can infiltrate or displace white matter fiber tracts, MS lesions do not necessarily influence the localization or structure of axonal fibers. Rather, the lesions and the corresponding de- and remyelination may influence the diffusion parameters along the fibers (Fink et al., 2009). Thus, for both groups, we perform FT of bundles of interest, i.e., bundles near the tumor or bundles which can be influenced by lesions. In the case of tumor patients, we mainly focused on qualitative comparisons and visually compared the results in order to assess the differences. Furthermore, we determined the volume of a sheath which wraps the fibers in order to estimate the differences. For the MS patients, we also performed a quantification of several DTI parameters along the tracked bundles.

In the following, we briefly describe the FT algorithms implemented in MeVisLab, our research and development platform (MeVisLab 2.0, 2010) which we used for comparison purpose. Our probabilistic Bayesian approach (Friman et al., 2006) is well-studied and has been used by several other authors, such as (Oguz et al., 2009). Thus, this approach is our first choice for probabilistic FT. The necessary modeling and estimation of fiber orientation and connection can be described at both global and local levels. At the global level, a theoretical foundation for estimating the probability of a connection between two areas in the brain has

been given. At the local level, probability density functions of the fiber orientation can be derived in a theoretically justified way via Bayes' theorem. In addition, a theorem has been integrated that facilitates the estimation of parameters in a constrained version of the popular tensor model of water diffusion.

Although we have fully parallelized the Bayesian approach, its high computation time inhibits use in routine clinical tasks. Thus, we propose another approach for FT similar to bootstrapping methods (Chung et al., 2006; Jones et al., 2005), but which is faster and does not need several repetitions of the diffusion-weighted images. The method, which we have named variational noise FT, allows an efficient computation of diffusion-weighted images with user-defined noise while retaining the MRI noise characteristics. The essential idea is to add complex Gaussian noise to the magnitude images (Hahn et al., 2006) and to track the fibers for each artificially computed diffusion-weighted data set.

For a fair comparison between both probabilistic approaches, the noise of the diffusion-weighted images used for the Bayesian method should match the noise of the images computed by the variational noise technique.

The deterministic FT algorithm which we use (Schlueter et al., 2005) to compare with both probabilistic approaches is based on the deflection-based approach by (Weinstein et al., 1999) and makes use of the full diffusion tensor information during tracking. In contrast, commonly employed streamline-based algorithms, such as the FACT (fiber assignment by continuous tracking) method (Mori et al., 1999), only consider the largest eigenvector representing the main diffusion direction. In comparison to the method described in (Weinstein et al., 1999), we added a moving average estimation of the fiber curvature and anisotropy to the tracking algorithm, which leads to more accurate tracking dynamics and more robust termination criteria.

### 3.1 Qualitative comparisons of fiber tracking (glioma patients)

For the qualitative analysis, magnetic resonance images of tumor patients were obtained using a 3T scanner (Siemens Trio, Erlangen, Germany). The subjects were supine and a head coil with a circularly polarized array was used with 2D DTI echo planar imaging, 12 diffusion directions and 5 repetitions. The sequence parameters were: repetition time (TR) 6400 msec, echo time (TE) 91 msec, field of view (FOV) 240 mm, voxel size  $2.5 \times 2.5 \times 2.5 \text{ mm}^3$ , 50 slices, and scanning time of 8 minutes. Autoshimming and phase correction were activated.

From a large pool of data sets of glioma patients, we selected some patients for a qualitative comparison. All selected patients have progressive gliomas (grade 4) or progressive astrocytomas (grade 2) next to the pyramidal and the optical tracts. To track the pyramidal tracts, seed regions within the capsula interna were chosen, while for tracking the optical tracts, seed regions in the occipital lobe were used. In all cases, exclusion ROIs (regions of interest) were used to discard unwanted fibers. Moreover, we propose to measure the volume of the sheath that encloses the single fiber tracts. To compute the sheath, we propose a neighboring cells algorithm based on the well-known marching cubes algorithm with which a volume (image) is scanned by discretization into cells. The necessary input volume is determined by voxelizing the 3D fiber tracts.

Some of the qualitative results can be found in Fig. 1. In nearly all cases, both probabilistic approaches are superior to the deterministic algorithm. In particular, fibers at the marginal regions of the white matter are more precisely tracked if the probabilistic algorithms are used. Consequently, the sheath volumes differ substantially for the different algorithms (probabilis-

tic results are about 30% higher on average). The differences between the variational noise tracking approach and the Bayesian approach are very small for all patients.

### 3.2 Quantitative comparisons of fiber tracking (multiple sclerosis patients)

For the quantitative analysis, magnetic resonance images of relapsing-remitting MS patients and healthy controls (10 patients, 10 healthy volunteers) were obtained using a 1.5T scanner (Siemens Avanto, Erlangen, Germany). The subjects were supine and a head coil with a circularly polarized array was used with 2D DTI echo planar imaging, 30 diffusion directions and 2 repetitions. The sequence parameters were: repetition time (TR) 8000 msec, echo time (TE) 100 msec, field of view (FOV) 230 mm, voxel size  $2.0 \times 2.0 \times 2.7\text{mm}^3$ , 55 slices, and a scanning time of 8 minutes. Autoshimming and phase correction were activated.

We have tested both the deterministic and the probabilistic FT (Bayesian) to determine whether and how they allow the detection of differences of diffusion-derived parameters between relapsing-remitting MS patients and healthy controls (10 patients, 10 healthy volunteers). For that purpose, we decided to quantify the superior longitudinal fasciculus (SLF) which has already been shown to be a structure for which differences between MS patients and healthy volunteers can be determined very well using deterministic FT (Fink et al., 2009). After extracting the right and left SLF, diffusion-derived parameters such as the FA, axial diffusivity, radial diffusivity, and diffusion strength were obtained along the tracts, and average values were computed. Then these values were recoded linearly to better permit statistical examination. For extracting the SLFs, only fiber tracts were considered which were included by two crop ROIs and values were only computed between those two crop ROIs. More precisely, each fiber is resampled so that all fibers consist of  $n$  equidistantly distributed fiber points. Using the resampled fibers, an average center line is computed, used to determine  $n$  reference planes depending on the local curvature of the center line. Afterwards, a reference plane is used to determine an average diffusion value at a certain position of the bundle by considering one diffusion value per fiber with the nearest distance to that plane.

The number of fibers of the probabilistic tracking has been aligned with the number of fibers of the deterministic tracking. This process occurs before the tracked structure has been cropped to the focus of interest in the SLF to ensure a valid comparison of the parameters after cropping. Furthermore, common parameters such as minimal FA must be adjusted for both algorithms.

The quantitative results can be found in Tab. 1 and Tab. 2. In two of the MS cases, fiber tracts could not be determined between both crop ROIs by the deterministic approach. Thus, these two cases were discarded. We used analysis of variance (ANOVA) through GLM (general linear model) for repeated measurements to analyze the sensitivity of the deterministic and the probabilistic method for pathological alterations in the MS patients. The FA and ADC values of the SLF left and the SLF right were used as dependent variables. The patient versus healthy control status is used as independent variable (between-subject factor), the hemisphere and the type of algorithm (deterministic/probabilistic) as within-subject factors. For the ADC values, there is a main effect for the cerebral hemisphere [ $F(1,16)$ : 11.027,  $p < 0.01$ ], a main effect for the algorithm used (deterministic vs. probabilistic) [ $F(1,16)$ : 4.444,  $p = 0.05$ ] and a significant interaction between algorithm used and patient groups [ $F(1,16)$ : 4.444,  $p = 0.05$ ]. Moreover, the independent group factor is also significant [ $F(1,17)$ : 12.085,  $p < 0.01$ ].

Patients had higher ADC values than healthy controls (3.625 vs. 2.25), right hemisphere ADC values are higher than left hemisphere ADC values (3.194 vs. 2.681), in healthy controls the ADC values did not differ between deterministic and probabilistic algorithm (2.25 vs. 2.25),

but in patients the probabilistic model yielded higher values than the deterministic algorithm (3.75 vs. 3.5). Note that these values are not the empiric data itself, but estimated marginal means, thus error-corrected values based on our empiric data.

For the FA values, the only significant effect is a main effect for the cerebral hemisphere [F(1,16): 5.47,  $p = 0.03$ ].

The number of fibers after the cropping varies widely not only between different persons, but also between hemispheres of the same brain. Statistics show that the probabilistic algorithm tracks an average of 254 fibers (SD=199), whereas the deterministic algorithm tracks an average of 188 fibers (SD=167). The standard deviation is high, that it seems impossible to interpret these results at first glance. However, the correlation between the probabilistically and deterministically gained numbers of fibers, found by Pearson test to be 0.89, shows that the trend between the algorithms is congruent. This indicates that the variance of the number of fibers is not due to the type of algorithm or chance, but primarily due to the underlying image data. Additionally, this highly variant but congruent trend indicates a high sensibility towards inter-individual differences in image data and demonstrates reliable algorithms.

	FA (prob.)	FA (det.)	ADC (prob.)	ADC (det.)
mean (right)	0.4130	0.4120	0.000716	0.000717
stddev (right)	0.0285	0.0311	$2.84 \cdot 10^{-5}$	$2.58 \cdot 10^{-5}$
mean (left)	0.4190	0.4170	0.000692	0.000692
stddev (left)	0.0300	0.0352	$2.89 \cdot 10^{-5}$	$2.69 \cdot 10^{-5}$

Table 1. Control group. FA: fractional anisotropy, ADC: diffusion strength.

	FA (prob.)	FA (det.)	ADC (prob.)	ADC (det.)
mean (right)	0.3680	0.3740	0.000810	0.000809
stddev (right)	0.0405	0.0390	$7.36 \cdot 10^{-5}$	$7.74 \cdot 10^{-5}$
mean (left)	0.3900	0.3910	0.000771	0.000767
stddev (left)	0.0403	0.0416	$7.53 \cdot 10^{-5}$	$7.33 \cdot 10^{-5}$

Table 2. MS patients. FA: fractional anisotropy, ADC: diffusion strength.

### 3.3 Discussion

Our qualitative results have shown that both probabilistic approaches are superior for tracking fibers near tumors or MS lesions with respect to completeness, quality and coverage of anatomical structures at their borders. Under the condition that all approaches are parameterized so that they track the same initial number of fibers, the probabilistic approaches are able to compute more fibers that pass two distant crop ROIs, indicating that fewer fibers were aborted during the fiber tracking process. The variational noise fiber tracking produces qualitatively very similar results compared to the Bayesian approach, but is computationally less expensive, thus, enhancing its appeal for clinical applications.

The quantitative results in combination with the qualitative results have shown that the probabilistic fiber tracking is more sensitive than the deterministic approach, especially if measuring the ADC values. The statistically significant interaction effect for ADC values between the

algorithm used (probabilistic/deterministic) and the health status results from the fact that on one level of the between-subjects factor (healthy volunteers) the algorithm used has no influence on the ADC scores, on the other level (patients) it influences the values. One can interpret this effect as a brain anatomy related effect of the algorithms used to generate the ADC values. The normal or more ideal brain anatomy of healthy volunteers allows less differentiation between the methods than does the pathological brain anatomy of patients. For quantification, we concentrated on one important fiber structure, the SLF, however, samples of other structures have shown similar results.

It is advisable to combine the quantitative and qualitative results to obtain an overall picture. For example, some MS patients could not be added to the quantitative analysis because only the probabilistic algorithm is able to produce processable results. This indicates that in clinical cases with brain lesions or neuronal diseases, the probabilistic algorithm is the method of choice. Although first papers have already proposed to implement probabilistic approaches on the GPU (McGraw & Nadar, 2007), this field of research should be examined in the future as probabilistic approaches are still an order of magnitude slower than deterministic solutions.

#### **4. Assessing Fiber Tracking Accuracy via Diffusion Tensor Software Models**

One of the major hurdles when developing fiber tracking algorithms is that hardware or software models of fiber bundles are needed in order to assess their validity and precision. It is therefore necessary to develop phantoms with a known fiber network. Software models have the advantage that they can be easily modified to account for different scanner parameters, image noise or artifacts. While much of the previous work has focused on simple phantoms in which fiber bundles were represented as cylindrical tubes or helices (see for example (Fieremans, De Deene, Delpitte, Ozdemir, D'Asseler, Vlassenbroeck, Deblaere, Achten & Lemahieu, 2008; Gössl et al., 2002; Lori et al., 2002)), in this section we suggest a framework in which it is possible to realistically model specific neural fiber bundles, simulating both the smooth transition between the actual white matter pathway and the surrounding tissue and the partial volume effects caused by the possible contemporary presence of white matter, grey matter and cerebrospinal fluid in one voxel.

We focus on generating a phantom of the corticospinal tract. Afterwards, we reconstruct the modeled tract by means of a fiber tracking algorithm and make a quantitative analysis of the algorithm's accuracy. This information is used to estimate what an appropriate safety margin around the tracked fibers should be and to analyze after which length the first fibers start to leave the modeled fiber bundle. Lastly, we suggest an efficient algorithm to construct safety hulls around the tracked fibers.

##### **4.1 DTI Model Framework**

In this section, we start by introducing the general framework that we use to generate the diffusion tensor model. Next, we provide details on how we model different tissues and white matter pathways. After an accuracy analysis of the employed fiber tracking algorithm, we conclude by suggesting an algorithm to construct safety hulls around the tracked fibers.

In order to generate a synthetic tensor field, we start by computing a set of diffusion-weighted (DW) images (one image for each corresponding gradient direction). The diffusion-weighted signal is modeled according to the CHARMED model proposed in (Assaf & Basser, 2005; Assaf et al., 2004). This model contains a hindered extra-axonal compartment as well as a restricted intra-axonal compartment. We restrict ourselves to the hindered model, which

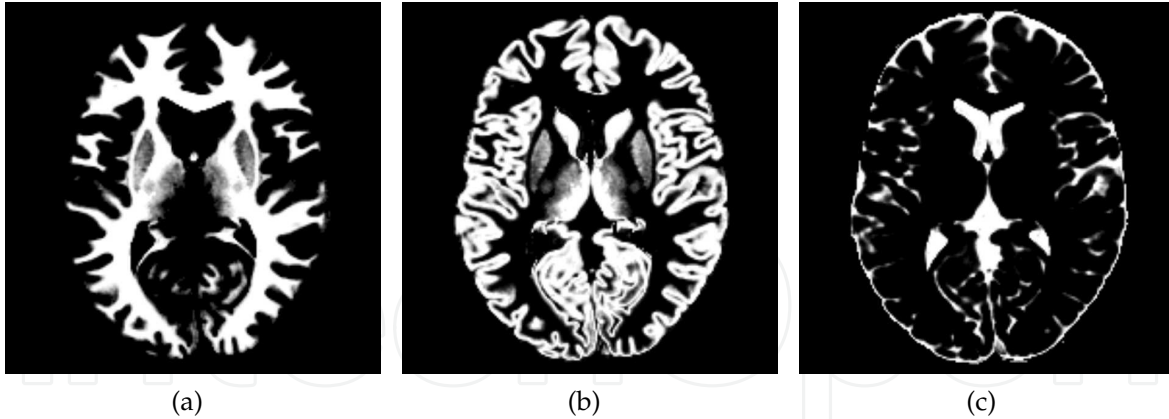


Fig. 2. (a): An example slice of the white matter volume. (b): The grey matter volume. (c): The cerebrospinal fluid volume.

gives rise to an effective diffusion tensor and primarily explains the Gaussian signal attenuation observed at low  $b$  values. Let us denote the diffusion time by  $\Delta$  and set

$$\mathbf{q} = \frac{\gamma \mathbf{g} \delta}{2\pi}$$

Here  $\gamma$  is the proton gyromagnetic ratio,  $\mathbf{g}$  is the vector whose magnitude is the strength of the applied diffusion gradient and whose direction is along the axis of the applied diffusion gradient,  $\delta$  is the width of the diffusion pulse gradient. In this case, the net signal attenuation is given by

$$E(\mathbf{q}, \Delta) = \sum_{i=1}^M f_h^i \cdot E_h^i(\mathbf{q}, \Delta) \quad (1)$$

where the  $f_h^i$  are the  $T_2$  weighted volume fractions of the hindered compartments,  $E_h^i(\mathbf{q}, \Delta)$  is the normalized MR echo signal from the  $i$ -th hindered compartment in a voxel. The CHARMED model assumes a cylindrically symmetric tensor model ( $\lambda_1 \neq \lambda_2 = \lambda_3$ ) and denotes the diffusion coefficients parallel and perpendicular to the axon's fiber by  $\lambda_{\parallel}$  and  $\lambda_{\perp}$  respectively. In similar manner,  $q$  may be written as  $\mathbf{q} = \mathbf{q}_{\parallel} + \mathbf{q}_{\perp}$ . For details on the computation of  $\mathbf{q}_{\parallel}$  and  $\mathbf{q}_{\perp}$  see (Assaf et al., 2004). Then  $E_h^i(\mathbf{q}, \Delta)$  is given by

$$E_h^i(\mathbf{q}, \Delta) = e^{-4\pi^2(\Delta - (\delta/3))|q_{\parallel}|^2\lambda_{\parallel}} + e^{-4\pi^2(\Delta - (\delta/3))|q_{\perp}|^2\lambda_{\perp}}$$

It is known that noise in magnitude magnetic resonance data is Rician distributed (Gudbjartsson & Patz, 1995). As suggested in (Hahn et al., 2006), such noise distribution may be simulated in the image by computing  $|E(\mathbf{q}, \Delta) + \tilde{N}(0, \sigma^2)|$ , where  $\tilde{N}(0, \sigma^2)$  is a Gaussian distributed complex variable with mean 0 and variance  $\sigma^2$ . Using standard fitting procedures, we use the DW images to compute the tensor valued image.

#### 4.2 A Model based on Simulated Brain Data

Given the framework presented in Section 4.1, we need to specify the fractions of tissue present in each voxel with the corresponding  $T_2$  and diffusion properties. To this end, we build upon the BrainWeb project at McGill University (Bra, n.d.; Collins et al., 1998). The

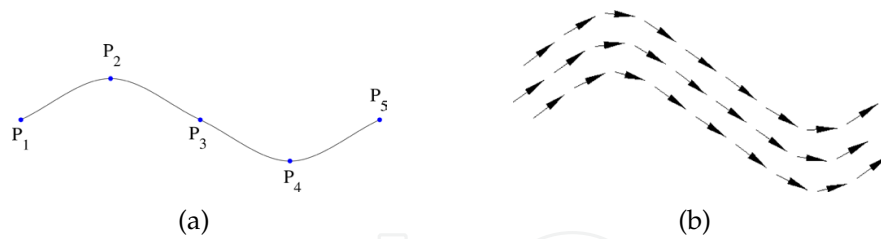


Fig. 3. (a): Example curve interpolating the control points  $\{P_i\}$  and forming the backbone of the modeled fiber bundle. (b): Schematic representation of the main diffusion directions of the tensors within the modeled fiber bundle.

BrainWeb project provides a dataset created by means of 27 low-noise scans ( $T_1$  weighted gradient echo acquisitions with  $TR/TE/FA = 18\text{ms}/10\text{ms}/30^\circ$ ) of the same individual, coregistered in stereotaxic space where they were subsampled and intensity averaged (Holmes et al., 1998). By means of a modified minimum-distance classifier, ten volumetric datasets that define the spatial distribution for different tissues were created. In these images, the voxel intensity is proportional to the fraction of tissue within the voxel. In our model we make use of the white matter, grey matter and cerebrospinal fluid volumes, an example slice of each volume is shown in Fig. 2. The volumes are defined at a 1mm isotropic voxel grid, with dimensions  $181 \times 217 \times 181$  (XxYxZ). Other tissue volumes that might be included in our model in later work include fat, skin, glial matter, and connective tissue.

To each fraction of tissue in a voxel we assign a main diffusion direction and the eigenvalues of the cylindrically symmetric diffusion tensor. The resulting signal attenuation is then computed according to Equation 1. For the above tissues, the average eigenvalues of the diffusion tensors have been measured and reported in (Bhagat & Beaulieu, 2004; Partridge et al., 2004; Pierpaoli et al., 1996), from which we derive the eigenvalues for our model written in Table 3. In case we do not model one or more white matter tracts to go through a voxel  $V$ , we assign a

	$T_2$ (ms)	$\lambda_{\parallel}$ ( $10^{-4}\text{mm}^2/\text{s}$ )	$\lambda_{\perp}$ ( $10^{-4}\text{mm}^2/\text{s}$ )
White Matter	70	$11.30 \pm 0.7$	$5.15 \pm 0.3$
Grey Matter	83	$9.90 \pm 0.4$	$7.05 \pm 0.3$
Cerebrospinal Fluid	329	$36.00 \pm 2.3$	$30.36 \pm 1.8$

Table 3.  $T_2$  values and tensor eigenvalues used in the BrainWeb-based model for the different tissues.

random main diffusion direction to each tissue portion present in  $V$ . However, we let the main diffusion directions corresponding to a given tissue type vary smoothly in space, in order to have, at least locally, a realistic change in tensor orientation.

Otherwise, if  $V$  has a white matter tissue portion and there are one or more fiber bundles going through it, the main diffusion direction depends on these bundles. Details on the modeling of fiber bundles and on setting the main diffusion direction are given in the following Section 4.3.

### 4.3 Modeling White Matter Pathways

In order to model a white matter pathway we start by defining a tuple of  $n$  control points  $\{P_i\}_{i=1,\dots,n}$  in  $\mathbb{R}^3$  through which the fiber bundle should go. To obtain a smooth backbone of

a fiber bundle from just a few control points, we perform cubic spline interpolation on  $\{P_i\}$ . For simplicity we choose Catmull-Rom splines, which are defined by two points  $P_i, P_{i+1}$  and two tangent vectors  $T_i, T_{i+1}$ . The tangent vectors are computed by

$$T_j = \frac{1}{2} \cdot (T_{j+1} - T_{j-1})$$

Then the evolution of the parametric curve  $s_i(t) = (x_i(t), y_i(t), z_i(t))^T$  with  $t \in [0, 1]$  and connecting  $P_i$  and  $P_{i+1}$  is given for example in  $x$ -dimension by

$$x_i(t) = \begin{pmatrix} t^3 & t^2 & t & 1 \end{pmatrix} \cdot \begin{pmatrix} 2 & -2 & 1 & 1 \\ -3 & 3 & -2 & -1 \\ 0 & 0 & 1 & 0 \\ 1 & 0 & 0 & 0 \end{pmatrix} \cdot \begin{pmatrix} P_{i_x} \\ P_{i+1_x} \\ T_{i_x} \\ T_{i+1_x} \end{pmatrix}$$

and similarly in the other dimensions. Concatenating the different splines  $\{s_i\}$  we have a differential 3D curve  $s$  connecting  $P_1$  to  $P_n$ . See Fig. 3(a) for an example curve.

Next, we resample the spline  $s$  at (small) equidistant  $t$  steps and obtain a final set of points which we denote by  $\{r_i\}_{i=1, \dots, N}$ . As suggested in (Leemans et al., 2005), we define a piecewise differential 3D space curve  $t(r)$ , which is 1 if  $r$  is on the backbone of the fiber and 0 else.  $t(r)$  is given by

$$t(r) = \sum_{i=1}^{N-1} \int_0^1 \delta[r - (r_i + \alpha \Delta_i)] d\alpha$$

where  $\delta$  denotes the Dirac-delta distribution and  $\alpha$  is a parametrization variable. To model the non-constant fiber density we convolve the fiber trajectory  $t(r)$  with a kernel  $k(r)$ :

$$T(r) = t(r) * k(r) = \sum_{i=1}^{N-1} \underbrace{\int_0^1 k[r - (r_i + \alpha \Delta_i)] d\alpha}_{\equiv T^i(r)}$$

Specifically we choose the saturated kernel

$$k(r) = \frac{\operatorname{erf}\left(\frac{w+2\|r\|}{2\sqrt{2}\sigma}\right) + \operatorname{erf}\left(\frac{w-2\|r\|}{2\sqrt{2}\sigma}\right)}{2 \operatorname{erf}\left(\frac{w}{2\sqrt{2}\sigma}\right)}$$

where  $\operatorname{erf}$  is the error function, the parameter  $w$  controls the width of the fiber bundle and  $\sigma$  controls the variance of the Gaussian decay.

We set the percentage  $P(r)$  of white matter occupied by the fiber in the voxel at  $r$  by

$$P(r) = \frac{T(r)}{\max_{r \in \mathbb{R}^3} T(r)}$$

The remaining white matter is modeled as having a random direction. In case there are several fibers which contribute to a voxel, we generally proceed as above, with the difference that we may have to rescale each contribution by the sum of all contributions, so that the latter sum is less or equal to one (100%).

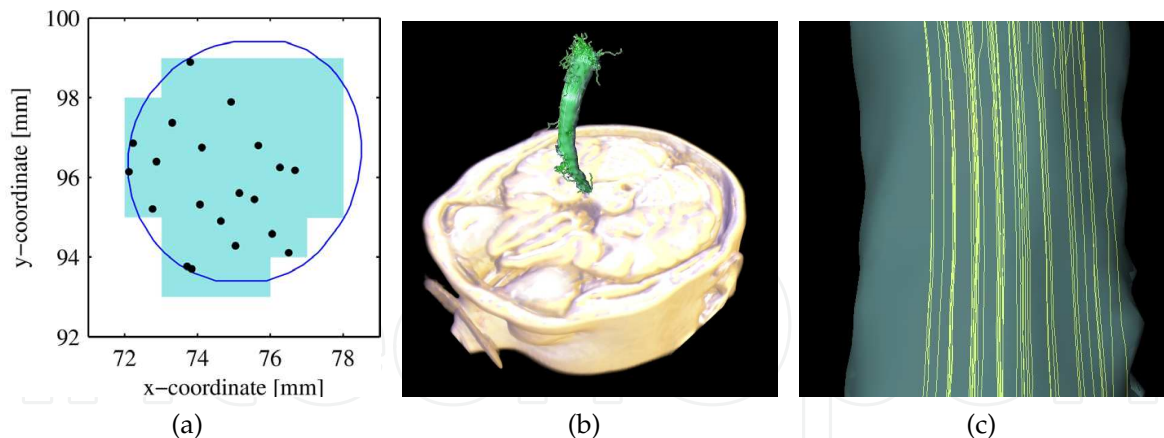


Fig. 4. (a): Cross section of the modeled corticospinal tract. The location of the tracked fibers is shown as dots. The voxels recognized by the safety-hull algorithm as part of the fiber bundle are overlaid in light blue. The parameters were  $T_{\text{dist}} = 4\text{mm}$ ,  $T_{\text{FA}} = 0.1$ ,  $T_{\text{BD}} = 0.07$ ,  $T_{\text{angle}} = 3^\circ$ . (b): Safety hull rendered with the tracked fibers. (c): Detail of the computed safety hull, showing its asymmetry with respect to the tracked fibers.

The main diffusion direction  $e_1$  of a fiber at  $r$  is computed as a weighted sum of the vector lines  $\Delta_i$ :

$$e_1(r) = \frac{\sum_{i=1}^{N-1} T^i(r) \Delta_i}{\left\| \sum_{i=1}^{N-1} T^i(r) \Delta_i \right\|}$$

A schematic representation of the main diffusion directions of the tensors is given in Fig. 3(b).

#### 4.4 Fiber Tracking Analysis

With the help of a physician having experience with DTI, we define the backbone of the right corticospinal tract. It is initially defined by 18 points and the parameters for the convolution kernel are  $w=12\text{mm}$  and  $\sigma=0.5$ . After resampling it consists of 968 points at a distance of 0.1mm. It is important to note that the thickness of a fiber bundle does not only depend on the kernel width, but also on the actual presence of white matter in the different voxels. After the fiber has been added to the model, we track it using the advection-diffusion based fiber tracking algorithm presented in (Schlueter et al., 2005), see also Section 3. In our implementation, the resulting tracked fibers are represented by several linearly connected points. To evaluate our algorithm, we compute the Hausdorff distance between one point of the spline-interpolated fiber backbone and the points of the tracked fibers. Given that the fibers are sampled densely enough, this distance provides a good approximation of the maximal distance between the fibers in the model and those that are tracked.

#### 4.5 An Algorithm to Compute Safety Hulls

In the previous sections we have suggested a way to generate DT software models of specific neural fiber bundles and to analyze the error of the tracked fibers. We are now going to suggest an efficient algorithm to better estimate the extent of a tracked fiber bundle. The resulting data will be visualized by means of hulls around the tracked fibers, which we will denote by "safety hulls". We test our algorithm both on the BrainWeb-based phantom and on the real magnetic resonance scans of a patient. The suggested algorithm to compute safety

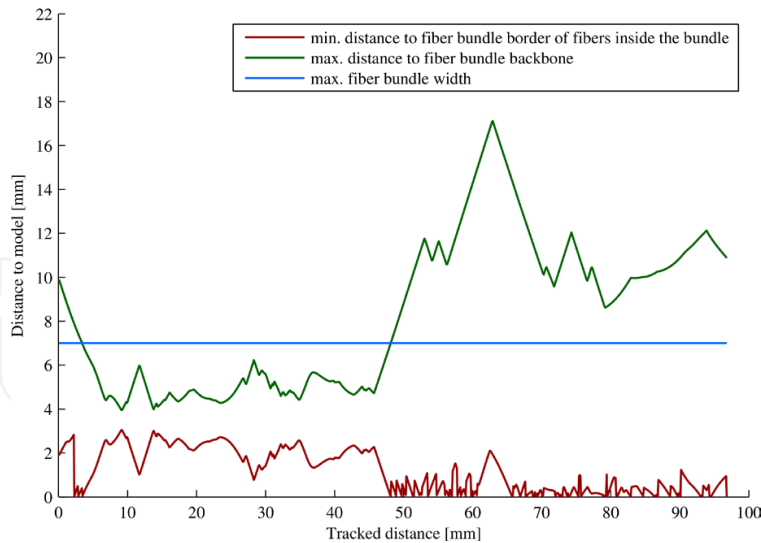


Fig. 5. Maximum distance between tracked fibers and modeled fiber bundle backbone.

hulls basically relies on dilating the tracked fibers if several threshold conditions are met. The algorithm proceeds as follows:

- Sample the tracked fibers and mark the image-voxels in which the sampled points lie. We will denote this set of voxels by  $\{V_i\}$ .
- For each voxel  $V \in \{V_i\}$  search in a  $n \times n \times n$  box centered at  $V$ . Out of this search box, mark a voxel  $\tilde{V}$  if it satisfies the following threshold conditions:
  - The distance between  $V$  and  $\tilde{V}$  should be smaller than  $T_{\text{dist}}$ .
  - The difference in FA between  $V$  and  $\tilde{V}$  should be smaller than  $T_{\text{FA}}$ .
  - The difference in bulk diffusivity (BD) between  $V$  and  $\tilde{V}$  should be smaller than  $T_{\text{BD}}$ .
  - The angle between the main diffusion directions of  $V$  and  $\tilde{V}$  should be smaller than  $T_{\text{angle}}$ .

We will denote the resulting larger set of Voxels by  $\{\tilde{V}\}_j$ .

- Denoising step: do a connected-component analysis on  $\{\tilde{V}\}_j$  and discard groups of voxels smaller than a predefined volume .
- For visualization purposes, fit a smooth surface to the resulting voxel set, giving the desired safety hulls.

In our inclusion criterion, the BD threshold is mainly used to differentiate between cerebrospinal fluid, tumor tissue, and regions of white or grey matter. On the other hand, FA has been shown to be highly heterogeneous in normal brain parenchyma and may be used as a criterion to differentiate between different white matter tracts. For measurements of tensor eigenvalues in the different brain regions and a detailed analysis we refer to (Bhagat & Beaulieu, 2004; Partridge et al., 2004; Pierpaoli et al., 1996). As far as the connected-component analysis step of the algorithm is concerned, we make use of 6-connectivity in 3D and discard groups of voxels with a volume smaller than 50ml.

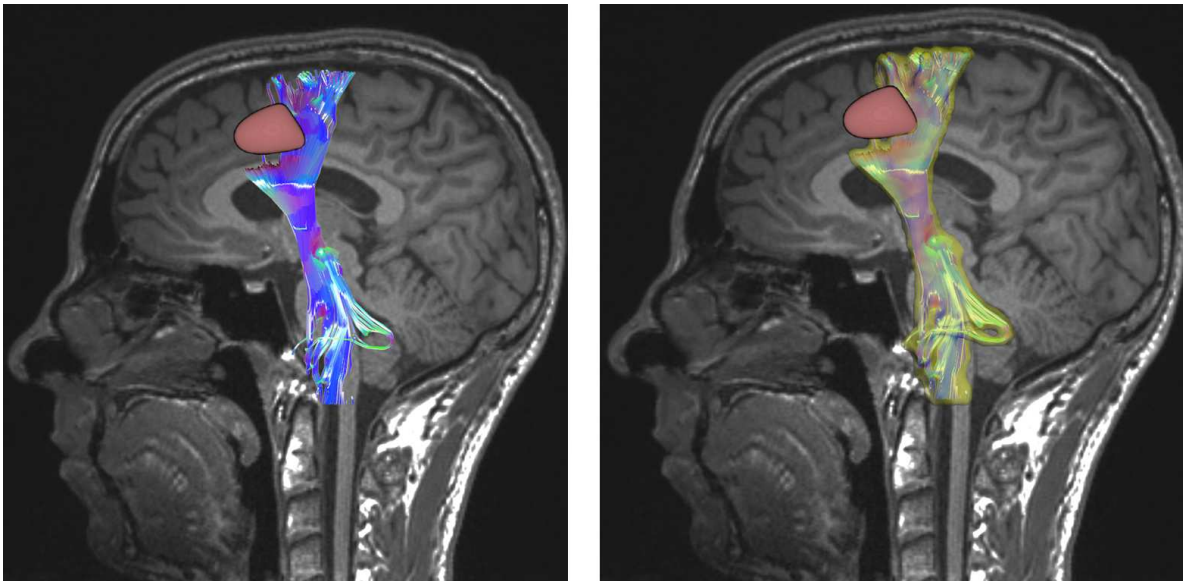


Fig. 6. Left: Tracked corticospinal tract of a tumor patient. The segmented tumor is shown in red. Right: Example visualization how margin around fibers can be visualized.

#### 4.6 Results

The remaining parameters used to compute the diffusion weighted images according to Equation 1 are reported in Table 4. We select a region at the level of the internal capsule to start

	Default value
voxel size	$1 \times 1 \times 1 \text{ mm}^3$
number of gradients	6
gradient strength	20 T/m
diffusion time	40 msec
pulse width	35 msec
gyromagnetic ratio	$2.675 \cdot 10^8 \text{ rad/sT}$
thermal noise variance	100
fiber tracking step length	1 mm

Table 4. Parameters used to compute the signal attenuation.

the tracking of the corticospinal tract. After the tracking, fibers which are obviously not part of the corticospinal tract are excluded from the result. Fig. 5 shows the tracked fibers and the distance plot. More in detail, the plot shows on one hand the maximum distance between fiber backbone and tracked fibers, on the other the minimum distance between fibers correctly tracked inside the bundle and the border of the bundle model (note that in the midbrain the latter distance may also be constrained by the actual presence of white matter).

We observe that fibers are tracked correctly inside the modeled fiber bundle between 3.5 and 48mm. Given that the fiber tracking seed was close to 25mm, this indicates that after a distance of approximately 20mm the first fibers leave the modeled bundle. When fibers are tracked correctly inside the bundle, the maximum distance to the fiber bundle border varies between 2 and 3mm, which this experiment indicates to be an appropriate safety margin. We start by

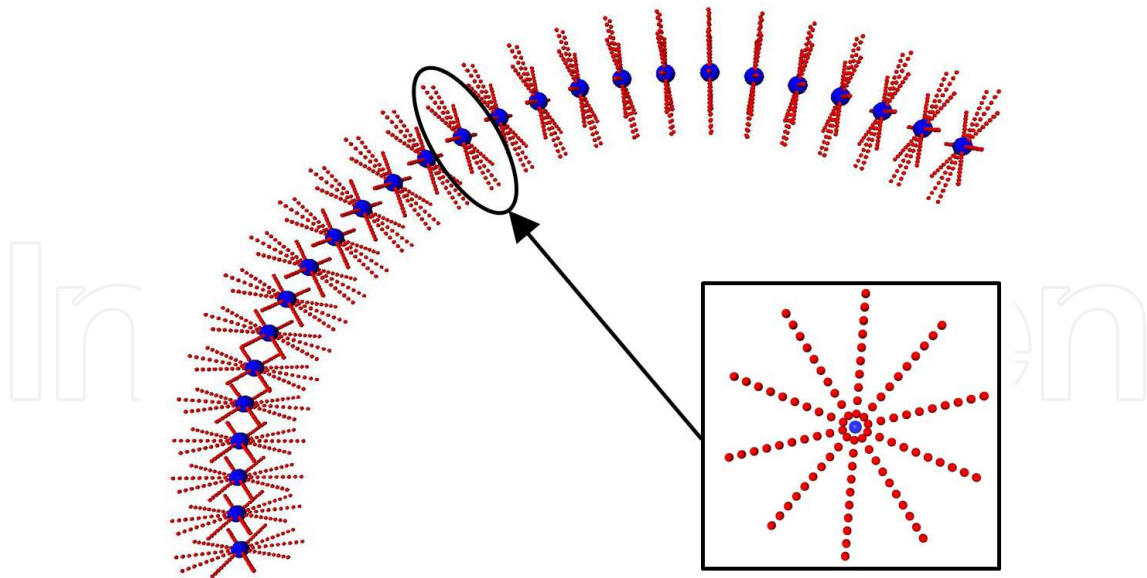


Fig. 7. The graph-based approach for estimating the boundary of fiber bundles, shown in Section 5, determines evaluation points around the calculated centerline of the bundle.

testing the safety hull generating algorithm on the tracked corticospinal tract from Section 4.2. The resulting hull is shown in Fig. 4. Particularly, from Fig. 4(c) we notice the asymmetry of the safety hull with respect to the tracked fibers. Finally, we test the algorithm on a real magnetic resonance dataset of a tumor patient (diffusion weighted images with TR/TE/FA = 6400ms/91ms/90°, voxel size is 2.5mm isotropic). The runtime of the algorithm was a few seconds on a QuadCore personal computer. Fig. 6 shows an example visualization how the safety hulls could be visualized.

#### 4.7 Discussion

In this section, we have described the creation of realistic DTI software models. These can be used as ground truth to test various fiber tracking algorithms. A first quantitative analysis of the advection-diffusion based fiber tracking algorithm suggests that, in the considered experiment, the first fibers leave the modeled bundle after approximately 20mm and that a safety margin of 2-3mm seems appropriate. Future work includes analyzing the precision of the algorithm in the presence of kissing or crossing fibers. We would also like to systematically analyze how precision varies in relation with the underlying image data (testing different values for image noise or artifacts, thickness of the fiber bundle, fractional anisotropy of the tensors) or in relation with fiber tracking parameters (such as step length, density of seed points). Moreover, fiber tracking results should be compared with those of other approaches, such as for example probabilistic ones. In the following Section 4.5, we suggested an algorithm to estimate the extent of a fiber bundle based on the tracked fibers and the underlying image data. The algorithm basically relies on dilating the tracked fibers if threshold conditions on voxel distance, FA, BD, and main diffusion direction difference are met. Results are visualized as semi-transparent hulls around the tracked fibers. The algorithm was tested both on one of our DTI phantoms and on a real magnetic resonance dataset. As with every parameter-dependent algorithm, the question of the optimal set of parameters arises, which shall be dealt with in the future. Ultimately, this work should help clinicians in better understanding the precision of generated fiber tracking results.

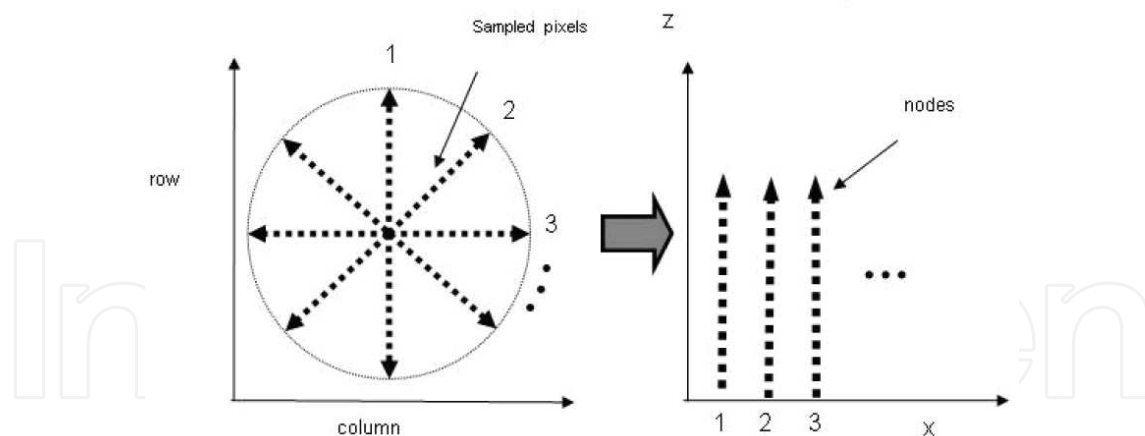


Fig. 8. Graph construction by unfolding of planes.

## 5. A Graph-based Approach for Boundary Estimation

Besides fiber tracking there are other approaches for fiber bundle segmentation and boundary estimation like volume growing (Merhof et al., 2005) or a graph-based min-cut segmentation depending on fractional anisotropy maps that will be discussed in the following section.

The segmentation starts with the choice of the fiber bundle for segmentation described by two manually placed regions of interest (ROIs) as start and end of the segmentation result. With the help of deflection based fiber tracking only tracked fibers within both ROIs are kept and cropped at the ROIs. Based on the resulting fibers a centerline of the fiber bundle is calculated like described by (Klein et al., 2007).

After the centerline calculation a set of evaluation points is created in the centerline's surrounding like shown in Fig. 7.

Therefore, the centerline is sampled at  $n$  points  $p_i, i \in [1..n]$ . For each of these point a plane upright to the local centerlines direction, given by  $p_{i+1} - p_i$  for  $i \in [1..n - 1]$  and  $p_n - p_{n-1}$  for  $i = n$ , is calculated. Within each of these planes  $l$  rays are sent out radially. Each ray is then sampled at  $m$  points with distance  $d$  between each of them. Each of this points is labeled with  $v_{i,j,k}$  where  $i \in [1..n]$  describes the plane,  $j \in [1..l]$  describes the ray within the plane and  $k \in [1..m]$  describes the evaluation point along the ray within the plane.

For the construction of the directed graph  $G = (V, E)$  the sampled planes are now unfolded in clockwise direction beginning with the ray at 12 o'clock like shown in Fig. 8 according to (Egger et al., 2009; 2008; Li et al., 2004a;b; 2006; Wu & Chen, 2002).

The set of nodes consists of all evaluation points  $v_{i,j,k}$  ( $i \in [1..n], j \in [1..l], k \in [1..m]$ ) and two additional nodes  $v_{sink}$  and  $v_{source}$ . The construction of weighted edges consists of different steps and is partly based on a cost function  $c(v_{i,j,k})$  for every node  $v_{i,j,k}$ . The used scalar cost function  $c(v_{i,j,k})$  is derived from the scalar fractional anisotropy maps of the underlying tensor data:

1. set  $E_1$  of  $\infty$ -weighted edges along a single ray:  

$$E_1 = \{(v_{i,j,k}, v_{i,j,k-1}) \mid i \in [1..n], j \in [1..l], k \in [2..m]\}$$
2. set  $E_2 = E_{2A} \cup E_{2B} \cup E_{2C} \cup E_{2D}$  of  $\infty$ -weighted edges between neighbored rays within a plane:  

$$E_{2A} = \{(v_{i,j,k}, v_{i,j+1, \max(0, k - \Delta_x)}) \mid i \in [1..n], j \in [1..l - 1], k \in [1..m]\}$$

$$E_{2B} = \{(v_{i,j,k}, v_{i,j-1, \max(0, k - \Delta_x)}) \mid i \in [1..n], j \in [2..l], k \in [1..m]\}$$

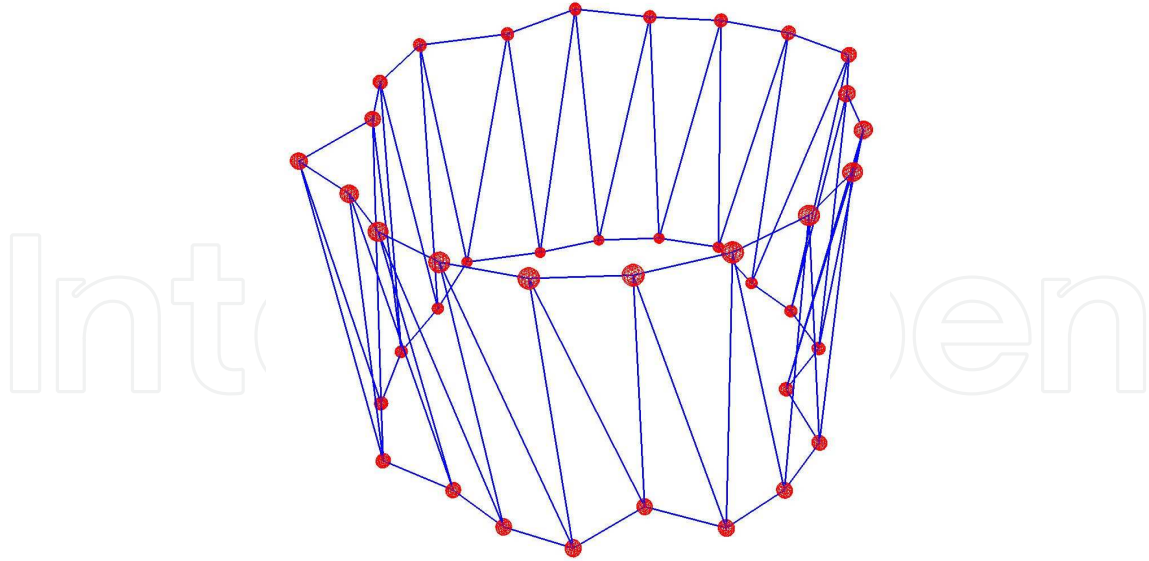


Fig. 9. Triangulation scheme for two neighbored evaluation planes.

$$E_{2C} = \{(v_{i,1,k}, v_{i,l,\max(0,k-\Delta_x)}) \mid i \in [1..n], k \in [1..m]\}$$

$$E_{2D} = \{(v_{i,l,k}, v_{i,0,\max(0,k-\Delta_x)}) \mid i \in [1..n], k \in [1..m]\}$$

3. set  $E_3 = E_{3A} \cup E_{3B}$  of  $\infty$ -weighted edges between neighbored planes:

$$E_{3A} = \{(v_{i,j,k}, v_{i+1,j,\max(0,k-\Delta_z)}) \mid i \in [1..n-1], j \in [1..l], k \in [1..m]\}$$

$$E_{3B} = \{(v_{i,j,k}, v_{i-1,j,\max(0,k-\Delta_z)}) \mid i \in [2..n], j \in [1..l], k \in [1..m]\}$$

4. set  $E_{st} = E_{source1} \cup E_{source2} \cup E_{sink1} \cup E_{sink2}$  of individually  $w$ -weighted edges to source and sink:

$$E_{source1} = \{(v_{i,j,1}, v_{source}) \mid i \in [1..n], j \in [1..l]\} \text{ with } w(i, j, 1) = c(i, j, 1)$$

$$E_{sink1} = \{(v_{i,j,m}, v_{sink}) \mid i \in [1..n], j \in [1..l]\} \text{ with } w(i, j, m) = c(i, j, m)$$

$$E_{source2} = \{(v_{i,j,k}, v_{source}) \mid i \in [1..n], j \in [1..l], k \in [2..m-1], c(v_{i,j,k}) - c(v_{i,j,k-1}) \geq 0\}$$

$$\text{with } w(i, j, k) = |c(v_{i,j,k}) - c(v_{i,j,k-1})|$$

$$E_{sink2} = \{(v_{i,j,k}, v_{sink}) \mid i \in [1..n], j \in [1..l], k \in [2..m-1], c(v_{i,j,k}) - c(v_{i,j,k-1}) < 0\} \text{ with}$$

$$w(i, j, k) = |c(v_{i,j,k}) - c(v_{i,j,k-1})|$$

The edges along the single rays ensure that all nodes below the surface are included to form a closed set. Thereby the interior of the fiber bundle can be separated from the exterior. The edges connecting different rays and planes constrain the set of possible segmentations. The two parameters  $\Delta_x$  and  $\Delta_z$  used for edge construction (see  $E_2$  and  $E_3$ ) enforce smoothness and stiffness of the result. The greater the parameters get, the greater is the number of possible segmentations.

After the graph construction, the minimal cost closed set is computed on the graph via a polynomial time s-t-cut (Boykov & Kolmogorov, 2001), creating an optimal segmentation of the fiber bundle, delivering a point set containing a boundary point for each ray of each plane. For comparison and evaluation a closed surface/volume of the segmented fiber bundle is needed. Due to the ordering of the point set given by the ordered construction of planes and rays, the point cloud can be triangulated easily. Therefore, neighbored contour point sets are triangulated like shown in Fig. 9. For volume construction the triangulated surface can be voxelized.

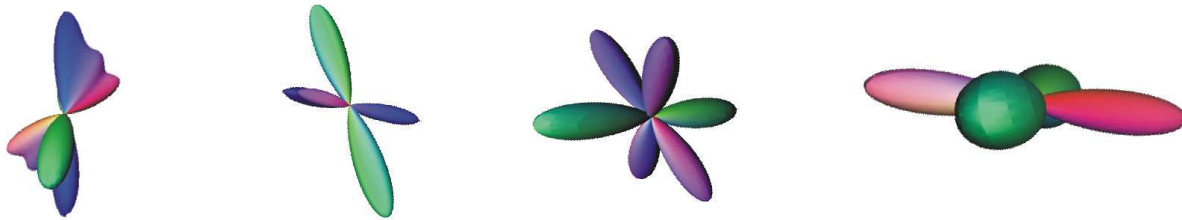


Fig. 10. Samples of an ODF visualization. The colors encode the directions, green: anterior/posterior, blue: cranial/caudal, red: lateral.

With the help of this surface/volume construction a comparison with other segmentation algorithms is possible. Also the evaluation of segmentation quality becomes possible by the use of phantoms with defined fiber tracts and corresponding masks for comparison like done in (Bauer et al., 2010) for example with the help of the Dice Similarity Coefficient (Zou et al., 2004).

## 6. Visualizing the Fiber Orientation Distribution Function

DTI does not provide a good basis for resolving fiber crossings or fiber kissings within a certain voxel due to underlying tensor model. Advanced approaches like q-space imaging may overcome this problem, however, the corresponding acquisition technique needs large field gradients and time-consuming sampling steps. Thus, these approaches are rarely used for clinical tasks. Q-Ball imaging (Tuch, 2004) tries to overcome this problem and reconstructs the HARDI signal model independently. Instead of minimizing a function of variables arising from a model, the orientation distribution function (ODF) is calculated directly from the signal by a Fourier transformation and a projection, which is actually approximated by the Funk-Radon-transform. The correct calculation assumes a gradient which approximates a  $\delta$ -distribution in time. Another possibility to reconstruct the ODF model-independently is to use spherical deconvolution (Tournier et al., 2004).

Fig. 10 shows ODF visualizations which may support the clinicians by assessing the uncertainty in the data and the fiber tracking algorithm. Because of not knowing the value of the ODF between the evaluated directions it is rather difficult to visualize the ODF as a surface without calculating many reconstruction points.

Our basic idea for visualizing an ODF is to map the reconstruction points to spherical coordinates by  $(\varphi, \theta) \in [0, 2\pi] \times [0, \pi]$ , which are afterwards inserted into a quadtree. The geometry of the quadtree can be used to build up a triangulation where the triangulation is refined at points with a high curvature of the corresponding surface. For that purpose, we split the quadtree according to the geodesic distances of two inserted reconstruction points on the sphere. Then, the algorithm can be formulated as follows:

1. Transform all reconstruction points in spherical coordinates via  $\phi : S^2 \rightarrow \mathbf{R}^3, (x, y, z) \mapsto (\cos^{-1}(z/r), \text{atan2}(y, x), 0)$ , where  $r := \sqrt{x^2 + y^2 + z^2}$  and  $S^2 := \{(x, y, z) \in \mathbf{R}^3 : \sqrt{x^2 + y^2 + z^2} = 1\}$

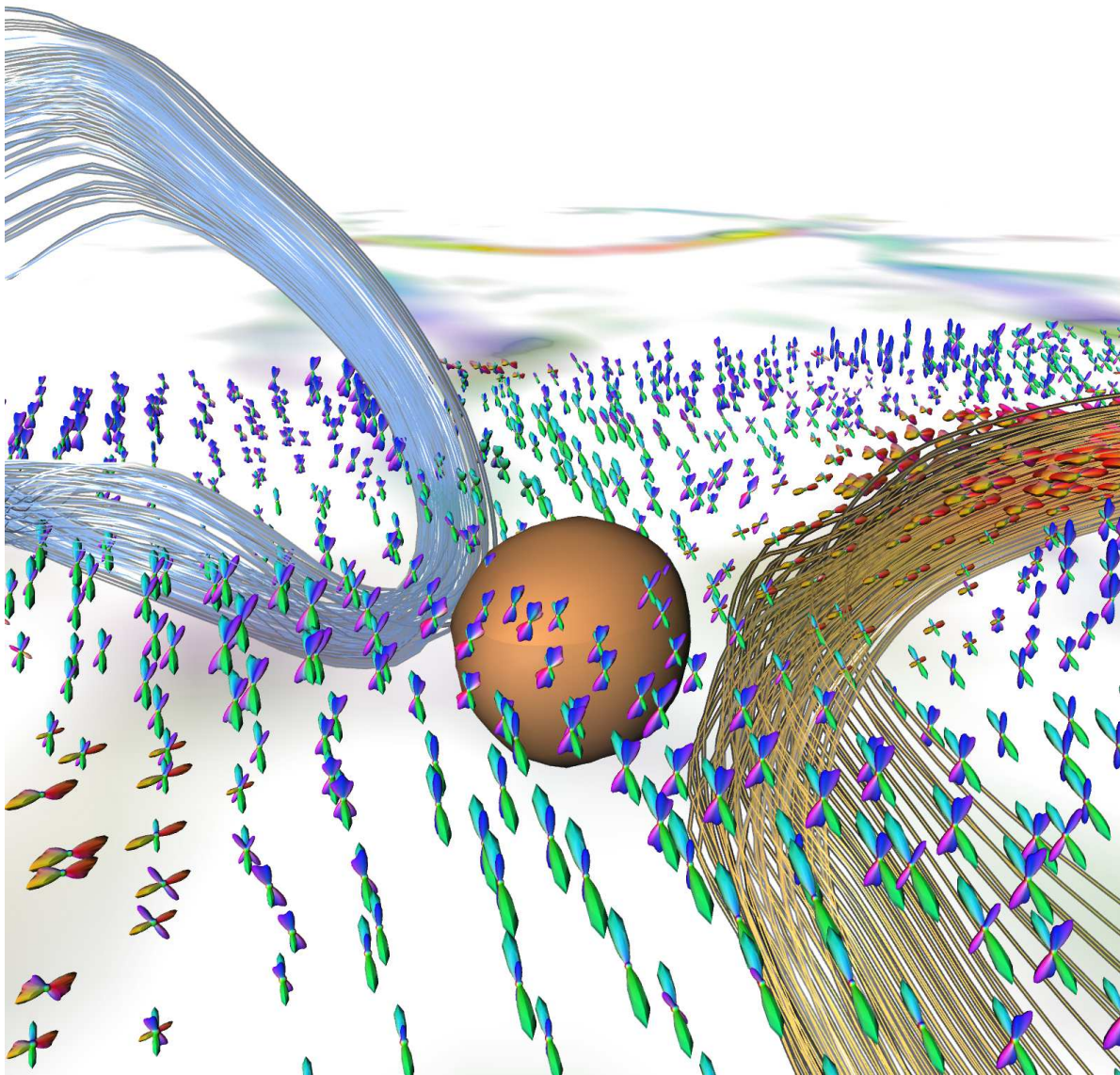


Fig. 11. Axial slice through the corpus callosum. The uncertainty of the fiber reconstruction can be assessed by visualizing the fiber orientation distribution function (fODF), which is a probability distribution on a sphere. The colors encode the directions, green: anterior/posterior, blue: cranial/caudal, red: lateral.

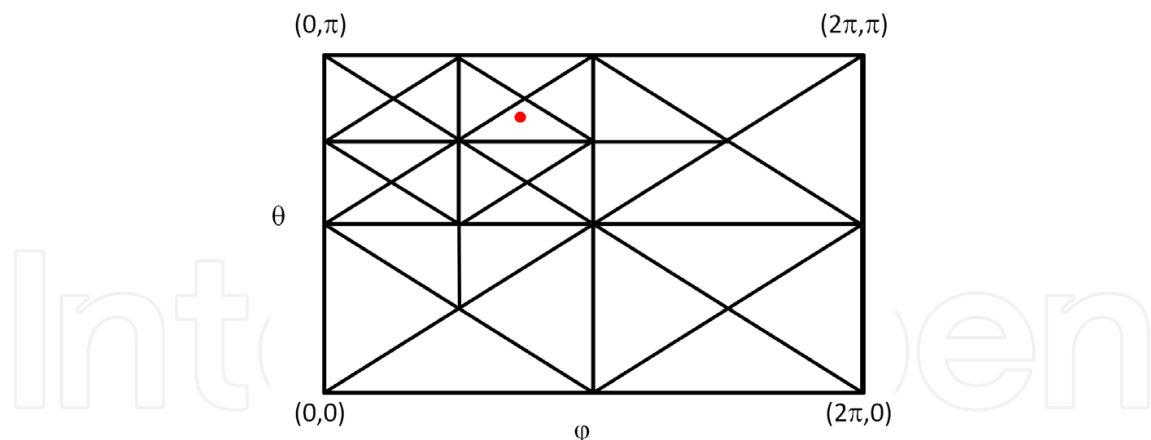


Fig. 12. Quad tree containing the adaptive triangulation of the plane. The cross marks an inserted direction.  $\varphi$  is on the x-axis and  $\theta$  on the y-axis.

2. Insert the reconstruction points  $d_i$  which have a diffusion which is more than  $\sigma$  away from the mean. Insertion means setting the z-component to the odf's value
3. Split the quad tree recursively until the bounding volumes have satisfied an error condition (this is in general a function  $\epsilon(d_1, \delta_1, \dots, d_n, \delta_n) \mapsto \mathbf{R}^+$ , where  $\delta_i$  is the distance of the quad to the inserted direction  $d_i$ . For computing the distance, we use the minima of geodesic distances of the vertices and the mid point to the inserted reconstruction point.
4. Insert additional vertices to avoid visual artifacts. This is done if a neighbor bounding volume has been split more often.
5. Map the plane to a sphere via  $\phi^{-1}(\theta, \varphi, r) \mapsto r(\cos \varphi \sin \theta, \sin \varphi \sin \theta, \cos \theta)$

Using this algorithm, which considers the metric of a sphere, the splitting leads to a good triangulation, also for small radii (small diffusion).

## 7. Conclusion

Technical challenges like improved spatial resolution, whole brain coverage, signal to noise ratio, or magnetic susceptibility artifacts constitute the basis for reliable quantification techniques in diffusion neuroimaging. For example, high-resolution 3D imaging sequences facilitated by parallel imaging will strongly contribute towards quantitative reliability. Still, in most cases, partial volume modeling will be key to yield highly reliable quantitative measurements due to the complexity or small spatial extent of both anatomical features and pathological alterations. For example, there is increasing evidence that subtle or even significant gray matter alterations play an important role in MS pathology (Zivadinov & Cox, 2007). Furthermore, preprocessing algorithms for registration, regularization, or outlier rejection are substantial influencing factors.

In the case of quantitative DTI, the assumption of a Gaussian diffusion process may not be adequate in areas of complex fiber structures like crossing or kissing fibers not only for fiber reconstruction but also for quantitative assessment. This problem has recently been addressed by multiple-compartment models, diffusion spectrum imaging, spherical deconvolution and persistent angular structure MRI (PAS-MRI), where higher order tensors or probability distributions describe the actual diffusion process. (Assaf et al., 2002) have already shown that

with q-space imaging the difference of values in the normal appearing white matter of patients with multiple sclerosis is more pronounced than with DTI. However, virtually all techniques based on HARDI data are still in an early state and are subject to improvement with respect to acquisition and postprocessing time so that they become useful for clinical routine. We have given several examples in the context of diffusion neuroimaging where quantification techniques play an important role and have presented and discussed software and hardware phantoms for measuring their precision and reliability. Without such evaluation basis, several pitfalls and systematic errors might remain undetected.

## 8. References

- Assaf, Y. & Basser, P. J. (2005). Composite hindered and restricted model of diffusion (CHARMED) MR imaging of the human brain, *Neuroimage* **27**: 48–58.
- Assaf, Y., Ben-Bashat, D., Chapman, J., Peled, S., Biton, I., Kafri, M., Segev, Y., Hendler, T., Korczyn, A., Graif, M. & Cohen, Y. (2002). High b-value q-space analyzed diffusion-weighted mri: Application to multiple sclerosis, *Magnetic Resonance in Medicine* **47**(1): 115–126.
- Assaf, Y., Freidlin, R. Z., Rohde, G. K. & Basser, P. J. (2004). New modeling and experimental framework to characterize hindered and restricted water diffusion in brain white matter, *Magn. Reson. Med.* **52**: 965–978.
- Barboriak, D. (2003). Imaging of brain tumors with diffusion-weighted and diffusion tensor mr imaging, *Magn Reson Imaging Clin N Am* **11**: 379–401.
- Basser, P. & Pajevic, S. (2003). Dealing with uncertainty in diffusion tensor MR data, *Israel Journal of Chemistry* **43**: 129–144.
- Basser, P., Pajevic, S., Pierpaoli, C. & Aldroubi, A. (2002). Fiber tract following in the human brain using dt-mri data, *IEICE Trans. Inf. & Syst.* **E85-D**(1): 15–21.
- Bauer, M. H. A., Egger, J., Barbieri, S., Klein, J., Freisleben, B., Hahn, H.-K. & Nimsky, C. (2010). A Fast and Robust Graph-based Approach for Boundary Estimation of Fiber Bundles Relying on Fractional Anisotropy Maps, *Proceedings of the 20th International Conference on Pattern Recognition (ICPR)*, Istanbul, Turkey, p. (to appear).
- Behrens, T., Woolrich, M., Jenkinson, M., Johansen-Berg, H., Nunes, R., Clare, S., Matthews, P., Brady, J. & Smith, S. (2003). Characterization and propagation of uncertainty in diffusion-weighted mr imaging, *Magnetic Resonance in Medicine* **50**: 1077–1088.
- Berman, J. I., Nagarajan, S. S., Berger, M. S. & Henry, R. G. (2004). Comparison of fiber tracking techniques in combination with functional localization in brain tumor patients, *Proceeding of ISMRM*, p. 1260.
- Bhagat, Y. A. & Beaulieu, C. (2004). Diffusion anisotropy in subcortical white matter and cortical gray matter: Changes with aging and the role of CSF-suppression, *Magn. Reson. Imaging* **20**: 216–227.
- Boykov, Y. & Kolmogorov, V. (2001). An Experimental Comparison of Min-Cut/Max-Flow Algorithms for Energy Minimization in Vision, *IEEE Transactions on Pattern Analysis and Machine Intelligence* **26**: 359–374.
- Bra (n.d.). Project URL: <http://www.bic.mni.mcgill.ca/brainweb/>.
- Chung, S., Lu, Y. & Henry, R. G. (2006). Comparison of bootstrap approaches for estimation of uncertainties of dti parameters, *NeuroImage* **33**(2): 531 – 541.
- Collins, A., Zijdenbos, A., Kollokian, V., Sled, J., Kabani, N., Holmes, C. & Evans, A. (1998). Design and construction of a realistic digital brain phantom, *IEEE Trans. Med. Imaging* **17**(3): 463–468.

- Egger, J., Freisleben, B., Setser, R., Renapuraar, R., Biermann, C. & O'Donnell, T. (2009). Aorta Segmentation for Stent Simulation, *12th International Conference on MICCAI, Cardiovascular Interventional Imaging and Biophysical Modelling Workshop*, London, United Kingdom.
- Egger, J., O'Donnell, T., Hopfgartner, C. & Freisleben, B. (2008). Graph-Based Tracking Method for Aortic Thrombus Segmentation, *Proceedings of 4th European Congress for Medical and Biomedical Engineering, Engineering for Health*, Antwerp, Belgium.
- Fieremans, E., De Deene, Y., Delputte, S., Ozdemir, M., Achten, E. & Lemahieu, I. (2008). The design of anisotropic diffusion phantoms for the validation of diffusion weighted magnetic resonance imaging, *Physics in Medicine and Biology* **53**: 5405–5419.
- Fieremans, E., De Deene, Y., Delputte, S., Ozdemir, M., D'Asseler, Y., Vlassenbroeck, J., Deblaere, K., Achten, E. & Lemahieu, I. (2008). Simulation and experimental verification of the diffusion in an anisotropic fiber phantom, *J. Magn. Reson.* **190**(1): 189–199.
- Fink, F., Klein, J., Lanz, M., Mitrovics, T., Lentschig, M., Hahn, H. K. & Hildebrandt, H. (2009). Comparison of diffusion tensor-based tractography and quantified brain atrophy for analyzing demyelination and axonal loss in ms., *J Neuroimaging*.
- Friman, O., Farneback, G. & Westin, C.-F. (2006). A Bayesian approach for stochastic white matter tractography, *IEEE Transactions on Medical Imaging* **25**(8): 965–978.
- Gössl, C., Fahrmeir, L., Pütz, B., Auer, L. & Auer, D. (2002). Fiber tracking from DTI using linear state space models: Detectability of the pyramidal tract, *Neuroimage* **16**: 378–388.
- Griffin, C., Chard, D., Ciccarelli, O., Kapoor, R., Barker, G., Thompson, A. & Miller, D. (2001). Diffusion tensor imaging in early relapsing-remitting multiple sclerosis, *Multiple Sclerosis* **7**(5): 290–297.
- Gössl, C., Fahrmeir, L., Pütz, B., Auer, L. & Auer, D. (2002). Fiber tracking from dti using linear state space models: detectability of the pyramidal tract, *Neuroimage* **16**(2): 378–388.
- Gudbjartsson, H. & Patz, S. (1995). The Rician distribution of noisy MRI data, *Magn. Reson. Med.* **34**: 910–914.
- Hahn, H. K., Klein, J., Nimsky, C., Rexilius, J. & Peitgen, H.-O. (2006). Uncertainty in diffusion tensor based fibre tracking, *Acta Neurochir Suppl* **98**: 33–41.
- Heiervang, E., Behrens, T., Mackay, C., Robson, M. & Johansen-Berg, H. (2006). Between session reproducibility and between subject variability of diffusion mr and tractography measures, *Neuroimage* **33**(3): 867–77. 1053-8119 (Print)Journal Article.
- Holmes, C., Hoge, R., Collins, D., Woods, R., Toga, A. & Evans, A. (1998). Enhancement of MR images using registration for signal averaging, *J. Comput. Assist. Tomogr.* **22**: 324–333.
- Inglis, B., Neubauer, D., Yang, L., Plant, D., Mareci, T. & Muir, D. (1999). Diffusion tensor mr imaging and comparative histology of glioma engrafted in the rat spinal cord, *AJNR Am J Neuroradiol* **20**: 713–716.
- Jones, D. (2003). Determining and visualizing uncertainty in estimates of fiber orientation from diffusion tensor MRI, *Magnetic Resonance in Medicine* **49**: 7–12.
- Jones, D., Travis, A., Eden, G., Pierpaoli, C. & Basser, P. (2005). PASTA: Pointwise assessment of streamline tractography attributes, *Magn. Reson. Med.* **53**: 1462–1467.
- Klein, J., Grötsch, A., Betz, D., Barbieri, S., Friman, O., Stieltjes, B., Hildebrandt, H. & Hahn, H. K. (2010). Qualitative and quantitative analysis of probabilistic and deterministic fiber tracking, *Medical Imaging 2010: Image Processing*, Vol. 7623, SPIE, pp. 76232A–1 – 76232A–8.

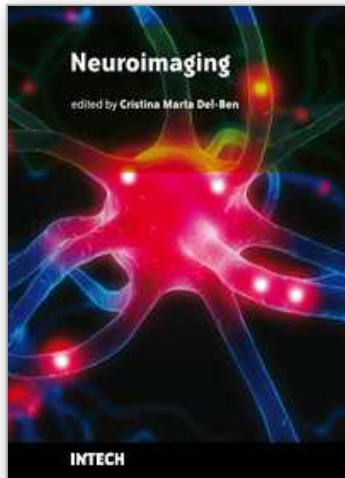
- Klein, J., Hermann, S., Konrad, O., Hahn, H. K. & Peitgen, H.-O. (2007). Automatic Quantification of DTI Parameters along Fiber Bundles, *Proceeding of Image Processing for Medicine (BVM 2007)*, pp. 272–2.
- Leemans, A., Sijbers, J., Verhoye, M., van der Linden, A. & van Dyck, D. (2005). Mathematical framework for simulating diffusion tensor mr neural fiber bundles, *Magnetic resonance in medicine* **53**(4): 944–953.
- Li, K., Wu, X., Chen, D. Z. & Sonka, M. (2004a). Efficient optimal surface detection: theory, implementation, and experimental validation, *Society of Photo-Optical Instrumentation Engineers (SPIE) Conference Series*, Vol. 5370 of *Presented at the Society of Photo-Optical Instrumentation Engineers (SPIE) Conference*, pp. 620–627.
- Li, K., Wu, X., Chen, D. Z. & Sonka, M. (2004b). Globally Optimal Segmentation of Interacting Surfaces with Geometric Constraints, *Proceedings of the IEEE CS Conf. Computer Vision and Pattern Recognition (CVPR)*, Vol. 1, pp. 394–399.
- Li, K., Wu, X., Chen, D. Z. & Sonka, M. (2006). Optimal Surface Segmentation in Volumetric Images-A Graph-Theoretic Approach, *IEEE Transactions on Pattern Analysis and Machine Intelligence* **28**(1): 119–134.
- Lin, C.-P., Tseng, W.-Y. I., Cheng, H.-C. & Chen, J.-H. (2001). Validation of diffusion tensor magnetic resonance axonal fiber imaging with registered manganese-enhanced optic tracts, *Neuroimage* **14**: 1035–1047.
- Lori, N., Akbudak, E., Shimony, J., Cull, T., Snyder, A., Guillory, R. & Conturo, T. (2002). Diffusion tensor fiber tracking of human brain connectivity: acquisition methods, reliability analysis and biological results, *NMR Biomed.* **15**: 493–515.
- McGraw, T. & Nadar, M. (2007). Stochastic dt-mri connectivity mapping on the gpu, *IEEE Trans. Vis. Comput. Graph.* **13**(6): 1504–1511.
- Merhof, D., Hastreiter, P., Nimsky, C., Fahlbusch, R. & Greiner, G. (2005). Directional Volume Growing for the Extraction of White Matter Tracts from Diffusion Tensor Data, *SPIE - Medical Imaging 2005: Visualization, Image-Guided Procedures, and Display.*, Vol. 5744, pp. 165–172.
- MeVisLab 2.0 (2010). Homepage at: <http://www.mevislab.de>.  
URL: <http://www.mevislab.de>
- Mori, S., Crain, B., Chacko, V. & van Zijl, P. (1999). Three-dimensional tracking of axonal projections in the brain by magnetic resonance imaging, *Ann Neurol.* **45**(2): 265–269.
- Nimsky, C., Ganslandt, O., Hastreiter, P., Wang, R., Benner, T., Sorensen, A. G. & Fahlbusch, R. (2005). Preoperative and intraoperative diffusion tensor imaging-based fiber tracking in glioma surgery, *Neurosurgery* **56**(1): 130–138.
- Oguz, I., Niethammer, M., Cates, J., Whitaker, R., Fletcher, T., Vachet, C. & Styner, M. (2009). Cortical correspondence with probabilistic fiber connectivity, *IPMI '09: Proceedings of the 21st International Conference on Information Processing in Medical Imaging*, Springer-Verlag, Berlin, Heidelberg, pp. 651–663.
- Partridge, S., Mukherjee, P., Henry, R., Miller, S., Berman, J., Jin, H., Lu, Y., Glenn, O., Ferriero, D., Barkovich, A. & Vigneron, D. (2004). Diffusion tensor imaging: serial quantitation of white matter tract maturity in premature newborns, *Neuroimage* **22**: 1302–1314.
- Pierpaoli, C., Jezzard, P., Basser, P., Barnett, A. & Di Chiro, G. (1996). Diffusion tensor MR imaging of the human brain, *Radiology* **201**: 637–648.
- Pul, C., Buijs, J., Vilanova, A., Roos, F. & Wijn, P. (2006). Fiber tracking in newborns with perinatal hypoxic-ischemia at birth and at 3 months, *Radiology* **240**(1): 203–214.

- Schlueter, M., Konrad, O., Hahn, H. K., Stieltjes, B., Rexilius, J. & Peitgen, H.-O. (2005). White matter lesion phantom for diffusion tensor data and its application to the assessment of fiber tracking, *Medical Imaging: Image Processing* **5746**: 835–844.
- Tournier, J.-D., Calamante, F., Gadian, D. G. & Connelly, A. (2004). Direct estimation of the fiber orientation density function from diffusion-weighted mri data using spherical deconvolution, *NeuroImage* **23**(3): 1176 – 1185.
- Tournier, J.-D., Yeh, C.-H., Calamante, F., Cho, K.-H., Connelly, A. & Lin, C.-P. (2008). Resolving crossing fibres using constrained spherical deconvolution: Validation using diffusion-weighted imaging phantom data, *Neuroimage* **42**(2): 617–625.
- Tuch, D. (2004). Q-ball imaging, *Magnetic Resonance in Medicine* **52**: 1358–1372.
- Weinstein, D. M., Kindlmann, G. L. & Lundberg, E. C. (1999). Tensorlines: Advection-diffusion based propagation through diffusion tensor fields, *VISUALIZATION '99: Proceedings of the 10th IEEE Visualization 1999 Conference (VIS '99)*, IEEE Computer Society, Washington, DC, USA, pp. 249–253.
- Wu, X. & Chen, D. Z. (2002). Optimal Net Surface Problems with Applications, *Proceedings of the 29th International Colloquium on Automata, Languages and Programming (ICALP)*, Malaga, Spain, pp. 1029–1042.
- Zivadinov, R. & Cox, J. (2007). Neuroimaging in multiple sclerosis, *Int Rev Neurobiol* **79**: 449–474.
- Zou, K. H., Warfield, S. K., Bharatha, A., Tempany, C. M. C., Kaus, M. R., Haker, S. J., Wells, W. M., Jolesz, F. A. & Kikinis, R. (2004). Statistical Validation of Image Segmentation Quality Based on a Spatial Overlap Index, *Academic Radiology* **11**(2): 178–189.

IntechOpen

IntechOpen

IntechOpen



## **Neuroimaging**

Edited by Cristina Marta Del-Ben

ISBN 978-953-307-127-5

Hard cover, 136 pages

**Publisher** Sciyo

**Published online** 17, August, 2010

**Published in print edition** August, 2010

Neuroimaging has become a crucial technique for Neurosciences. Different structural, functional and neurochemical methods, developed in recent decades, have allowed a systematic investigation on the role of neural substrates involved in functions performed by the central nervous system, whether normal or pathological. This book includes contributions from the general area of the neuroimaging to the understanding of normal functions and abnormalities of the central nervous system.

### **How to reference**

In order to correctly reference this scholarly work, feel free to copy and paste the following:

Jan Klein, Sebastiano Barbieri, Hannes Stuke, Miriam Bauer, Jan Egger, Christopher Nimsky and Horst Hahn (2010). On the Reliability of Diffusion Neuroimaging, *Neuroimaging*, Cristina Marta Del-Ben (Ed.), ISBN: 978-953-307-127-5, InTech, Available from: <http://www.intechopen.com/books/neuroimaging/on-the-reliability-of-diffusion-neuroimaging>

**INTECH**  
open science | open minds

### **InTech Europe**

University Campus STeP Ri  
Slavka Krautzeka 83/A  
51000 Rijeka, Croatia  
Phone: +385 (51) 770 447  
Fax: +385 (51) 686 166  
[www.intechopen.com](http://www.intechopen.com)

### **InTech China**

Unit 405, Office Block, Hotel Equatorial Shanghai  
No.65, Yan An Road (West), Shanghai, 200040, China  
中国上海市延安西路65号上海国际贵都大饭店办公楼405单元  
Phone: +86-21-62489820  
Fax: +86-21-62489821

© 2010 The Author(s). Licensee IntechOpen. This chapter is distributed under the terms of the [Creative Commons Attribution-NonCommercial-ShareAlike-3.0 License](#), which permits use, distribution and reproduction for non-commercial purposes, provided the original is properly cited and derivative works building on this content are distributed under the same license.

IntechOpen

IntechOpen